Phase transitions in the ferroelectric relaxor (1-x)$Pb(Mg_{1/3}Nb_{2/3})O_3$-x$PbTiO_3$ close to the morphotropic phase boundary

S. Kustov[1], J. Miguez Obrero[1], X. Wang[2], D. Damjanovic[3], E.K.H. Salje[4]

[1] Departament de Física, Universitat de les Illes Balears, cra Valldemossa km. 7.5, Palma de Mallorca, 07122, Spain

[2] Key Laboratory for Liquid-Solid Structural Evolution and Processing of Materials (Ministry of Education), Shandong University, Jingshi Road 17923, Jinan 250061, China

[3] Institute of Materials, Ecole Polytechnique Féderale de Lausanne, 1015 Lausanne, Switzerland

[4] Department of Earth Sciences, University of Cambridge, Downing Street, Cambridge CB2 3EQ, UK

Abstract

Structural transformations of unpoled (1-x)$Pb(Mg_{1/3}Nb_{2/3})O_3$-x$PbTiO_3$ (PMN-PT) single crystals (x=0.28 and x=0.32) were analysed by calorimetry and acoustic spectroscopy. The compositions are close to the morphotropic boundary (MPB). We find extended two-phase regions where cubic and rhombohedral (x=0.28), cubic and tetragonal, tetragonal and monoclinic phases (x=0.32) coexist during cooling and heating. The observed structural transitions in PMN-PT are first order, despite their proximity to the MPB. The predicted tricritical points, if they exist, are possibly located extremely close to the MPB.

Keywords: PMN-PT, calorimetry, acoustic spectroscopy, morphotropic boundary

1. Introduction

Phase diagrams of ferroelectric solid solutions containing morphotropic phase boundaries are subject of intense research [1-8]. A particular uncertainty relates to the nature and the topology of phase diagrams close to the morphotropic phase boundary (MPB). The sequence of the phase transitions often depends on the history of the sample, where even moderate polarizing field can change their phase stability. Phases close to the MPB were coined "fragile" [3]. Furthermore, the thermodynamic nature of the structural transitions is not always well defined as either second or weakly first order. Besides the knowledge of ferroelectric performance, the details of the structural transition range and the thermal hysteresis are also important for applications of ferroelectrics as shape memory materials [4], as in conventional metallic ferroelastics [5]. Rossetti et al. took $Pb(Zr_{1-c}Ti_c)O_3$ (PZT) as reference and used a Landau approach truncated to a 6^{th} order polynomial to describe structural phase transitions in relaxor ferroelectrics close to the MPB [2]. They concluded that the phase transition between the cubic (C), tetragonal (T) and rhombohedral (R) phase changes from second order close to the MPB to weakly first order at some distance from the MPB. The regions of the first and the second order phase transitions along the $C \leftrightarrow T$ and $C \leftrightarrow R$ line are potentially separated by tricritical points on both sides of the MPB. They located the MPB line at c_m^0=0.45 and the tricritical points at c_R^{cr}=0.30 and c_T^{cr}=0.60, suggesting they are well separated from the MPB composition. Thus, the region of the second order $C \leftrightarrow T$ and $C \leftrightarrow R$ transitions in PZT is expected to span the compositions between x(Ti)=0.30 and x(Ti)=0.60.

Coexistence of the C, T, R phases and occurrence of thermal hysteresis are indications of the first order transition[1], affecting the topology of the phase diagrams.

Experimental observations of the two-phase regions and the temperature hysteresis are sparse for ferroelectrics with MPBs, like PZT, $(1-x)Pb(Mg_{1/3}Nb_{2/3})O_3$-$xPbTiO_3$ (PMN-PT) and $(1-x)Pb(Zn_{1/3}Nb_{2/3})O_3$-$xPbTiO_3$ (PZN-PT). Experiments with unpoled PZT, PMN-PT, and PZN-PT samples are typically performed during cooling or heating [4-7, 10-21] not indicating and often not distinguishing these opposite scans [20,21]. The poled state is commonly investigated during heating [22]. The data on existence of tricritical points are controversial. Rossetti and Navrotsky [23] studied temperature hysteresis of specific heat peak in PZT ceramics with x(Ti)=1.00, 0.85, 0.0.70 and 0.60 and claimed that the hysteresis drops below

[1] We note that decreasing or vanishing of the thermal hysteresis does not necessarily imply approaching a tricritical point or second order transition and might be a consequence of nearing to the fulfillment of the cofactor crystallographic conditions during the first order ferroelastic ordering [9].

experimental resolution to ca. 0.6 K for the sample with x(Ti)=0.60, pointing to the existence of the tricritical point. However, their original data in Fig. 2 of Ref. [23] indicate that the hysteresis for x(Ti)=0.60 is the same as for x(Ti)=0.70, close to 6 K rather than 0.6 K. Fig. 4 of Ref. [23] indicates a saturation of the thermal hysteresis between x(Ti)=0.70 and x(Ti)=0.60 rather than its disappearance and the existence of the tricritical point close to x(Ti)=0.60. Solanki et al. [24] studied temperature hysteresis of permittivity and x-ray diffraction in Sr-doped PZT ceramics with x(Ti)=0.485-0.45 and claimed the existence of the tricritical point close to the triple point at x(Ti)≈0.45. However, their data showed non-zero hysteresis for x(Ti)=0.45 (Figure 2a of [24]), while fitting and extrapolation of the data that yielded a tricritical point at x(Ti)=0.447 were not clear. Noheda et al. [25] used Nb-doped ceramic PZT samples with x(Ti)=0.0, 0.03, 0.06, 0.09 and 0.22 to obtain the data on the temperature difference ΔT between a discontinuous jump in dielectric constant and extrapolated Curie point (for x(Ti) between 0.0 and 0.09) and on temperature hysteresis (for x(Ti)=0.22). The difference ΔT between the two characteristic temperatures decreased with x(Ti) for x(Ti) between 0.00 and 0.09, and the thermal hysteresis remained ca. 2 K for x(Ti)=0.22. Calculations according to effective field approach located a tricritical point as derived from the ΔT (for x(Ti) between 0.00 and 0.09) at x(Ti)≈0.26 [25]. The existence of the second tricritical point at x(Ti)=0.51 was also predicted [25]. Eremkin et al. [4] performed x-ray studies of the single crystalline PZT for the entire x(Ti) range between 1 and 0. They reported the triple point position at a rather low Ti content x(Ti)=0.22 due to the inclination of the MPB line towards Zr-rich side of the phase diagram. Two tricritical points along C-R and C-T lines at x(Ti)=0.22 and x(Ti)=0.55 were deduced from the extrapolation of the unit cell volume change and from the zero value of the uniform strain parameter, respectively. Unfortunately, as in other experimental works [24,25], the behaviour of the relevant parameters over a broad x(Ti) composition range in between two tricritical points has not been reported.

On the other hand, a large part of experimental results for PZT classify as the first order the C-T, C-R and R-T transitions for x(Ti) in between the expected tricritical points. A detailed study by Mishra et al. [26,27] was undertaken in PZT ceramic (x(Ti)=0.45-0.485), using lattice parameters [26], dielectric properties and piezoelectric resonance data [27] during heating and cooling. The authors located the MPB at x(Ti)=0.475 [26] and classified the $T \rightarrow C$ and $R \rightarrow C$ transitions on both sides of the MPB as stepwise. The jump of the lattice parameters was observed even at the MPB composition. The temperature hysteresis of the ferroelectric transition extended over 2 to 9 K for x(Ti)=0.485-0.450 [27]. Tricritical points

along C-T and C-R lines were not found in PZT. The authors [26,28] reported the two-phase R+T and M+T regions during crossing the MPB line, pointing to the first order of the $R \rightarrow T$ and $M \rightarrow T$ transitions as well. Yoon and Jang [29] studied the thermal hysteresis of the dielectric permittivity and the loss factor in pseudoternary $Pb(Ni_{1/3}Nb_{2/3})O_3$-$PbTiO_3$-$PbZrO_3$ (PNN-PT-PZ) and observed a change from the relaxor type to first order transition when the composition varied towards the tetragonal-rich side of the phase diagram. These authors described the stepwise $T \leftrightarrow R$ transition across the MPB. Low-frequency (0.1-1.0 Hz) internal friction and shear/Young´s modulus studies of PZT ceramics close to the x(Ti)=0.44, 0.46, 0.48 and 0.50 [6,15-17] reveal strong T-dot and frequency dependence of the low-frequency internal friction peak during $C \leftrightarrow T$ transition. The T-dot and frequency dependence is typical of the so-called transitory internal friction [30,31] that is a hallmark of a first order transition. Apart from the transitory origin of the phase transition internal friction term, Bouzid et al. [6] reported step-like variations of the elastic constants during $C \leftrightarrow T$ transition in PZT ceramics (x(Ti)=0.44, 0.46, 0.48 and 0.50), again discarding the existence of the tricritical points along C-T line over the ranges predicted in [2,4]. Cordero et al. [32] reported internal friction and elastic compliance measurements for four PZT ceramics (x(Ti)=0.455-0.53) at frequencies between 1 and 20 kHz. Thermal hysteresis of both $C \leftrightarrow T$ and $T \leftrightarrow R$ transitions, 3 K and up to 35 K, respectively was observed [32]. Calorimetry data for x(Ti)=0.48 PZT ceramic show thermal hysteresis of ca. 15 K [21] confirming the first order nature of $T \leftrightarrow R$ transition.

Reports of thermal hysteresis and two-phase regions in PMN-xPT are less abundant compared with PZT. This is possibly due to the complications related to the formation of polar nanoregions (PNR) and relaxor-type behaviour on the PMN-rich side of the phase diagram. The PMN-PT phase diagram for x between 0.30 and 0.39 (close to the MPB) was drawn by Noheda et al. [5] using synchrotron x-ray powder diffraction. The protocol of temperature variations was not indicated, but the position of the M_c-T phase boundary corresponded to the onset of the $M_C \rightarrow T$ transition [5]. Singh et al. [7] used piezoelectric resonance, dielectric properties and neutron diffraction data for PMN-xPT ceramics for x=(0.25-0.39) with steps of 0.01 to further elucidate the PMN-PT phase diagram. All phase transitions demonstrated step-like changes of the lattice parameters and coexistence of phases while the protocol of temperature variations was not specified.

In PMN-xPT, Algueró et al. [20] studied the temperature dependence of the Young´s modulus and damping for x=0.35 ceramics. However, as in the majority of studies, the authors did not indicate whether cooling or heating data were recorded. The same authors reported dielectric permittivity, low-frequency internal friction and Young´s modulus behaviour for polycrystalline PMN-xPT (x=0.2 and 0.3) [33]. They found a strong temperature hysteresis of the mechanical properties for x=0.2, corresponding to the C-R transition. The hysteresis between cooling and heating as seen in the dielectric properties was much less clear, however. Measurements of the Young´s modulus and damping using a low-frequency dynamic mechanical analyser and the dielectric properties of single crystalline PMN-0.29PT were performed by Yu et al. [34]. Low-frequency damping peaks during M-T and T-C transitions showed a clear transitory component, indicating their first order nature. No information whether cooling or heating data were shown was given (presumably, data taken on heating were reported). In conclusion, the PMN-PT phase diagram needs to be clarified for the following issues: (i) the existence and the location of the tricritical points; (ii) the magnitude of the thermal hysteresis; (iii) the width of the two-phase fields.

2. Material and methods

$Pb(Mg_{1/3}Nb_{2/3})O_3$-$xPbTiO_3$ single crystal plates ($3\times1\times25 mm^3$) with nominal compositions x=0.28 and x=0.32 were purchased from Atom Optics, Ltd. EDX check yielded x=0.285 (±0.018) and x=0.323 (±0.012) in reasonable agreement with the nominal compositions that will be used hereafter to identify the samples. All faces of the crystal were polished. The large surface was (100). The long sides of the plates were aligned along two <100> type directions. $1\times1\times12$ mm^3 rod-shaped samples for acoustic measurements were cut from the single crystalline plates using a low-speed diamond saw. The damaged parts of the lateral surfaces of the samples were removed using 4000 grit grinding paper. Small pieces of plates with masses close to 60 mg were used for DSC tests. (001) surfaces of the samples for dielectric measurements were covered with gold electrodes.

The piezoelectric ultrasonic composite oscillator technique [35-37] was used to measure the Young´s modulus (YM) and internal friction (IF) of the samples. The method employs longitudinal resonance at a frequency near 90 kHz of the oscillator consisting of two quartz transducers and a sample attached to them. The experimental arrangement [36,37] controls the strain amplitude of the oscillations ε_0, measures the internal friction (logarithmic decrement

δ_c) and the resonant frequency f_c of the oscillator. The internal friction δ and resonant frequency f of the sample are determined from the corresponding values for the assembled oscillator δ_c, f_c and for the quartz transducer alone, δ_q, f_q, using, respectively, the solutions from Refs. 35 and 38:

$$(m_s + m_q)\delta_c = m_s\delta + m_q\delta_q, \quad (1)$$

$$m_q f_q \tan\frac{\pi f_c}{f_q} + m_s f \tan\frac{\pi f_c}{f} = 0, \quad (2)$$

where m_s and m_q are the masses of the sample and of the quartz transducer alone, respectively. For the fundamental resonant mode, the YM of the sample, E, is determined from the resonant frequency f, the length of the sample l, and its density ρ:

$$E = 4\rho l^2 f^2. \quad (3)$$

Several experimental protocols were employed.

- Temperature spectra of the IF and YM were mostly measured at a low oscillatory strain amplitude ε_0 ca. 2×10^{-7} to avoid non-linear effects due to twin boundary movements.
- The IF dependence on strain amplitude was measured at room temperature to determine the linear and non-linear regimes.
- Some temperature spectra measurements for x=0.28 were performed with two strain amplitudes for each temperature point under cooling/heating rate of 1 K/min. The low strain amplitude ($\varepsilon_0^{low}=5\times10^{-7}$) was within the range of linear IF and YM behaviour, the high amplitude ($\varepsilon_0^{high}=4\times10^{-5}$) corresponded to the non-linear range. These experiments show simultaneously the temperature dependence of the linear $\delta_i(T)$ and the non-linear IF $\delta_h(T)$ via the difference between the spectra at high and low strain amplitudes.
- Measurements of temperature spectra with two strain amplitudes were repeatedly interrupted on cooling/heating and the kinetics of the linear and non-linear IF relaxation under isothermal conditions were measured.

DSC measurements were aimed at determining the characteristic transition temperatures and the ranges of phase coexistence and performed in a Mettler Toledo DSC3+. Samples with two masses (ca. 30 and 75 mg) were checked with two heating/cooling rates of 2 and 10 K/min. The transition temperatures obtained were the same within experimental error, discarding thus any detectable effect of thermal inertia of the calorimeter-sample system. DSC data for larger samples of ca. 75 mg (similar to the masses of the samples for acoustic and dielectric measurements) and 2 K/min cooling/heating rate are used. Dielectric permittivity and loss tangent $\tan\delta$ were measured between 1 and 100 kHz using an HP 4284 High Precision LCR meter. The samples were placed in a temperature controlled chamber and the driving voltage was 1 V_{rms} [39]. Polarized light observations of the microstructure were made with an Olympus BH2 optical microscope. Dielectric and acoustic measurements were performed for the same cooling/heating rate of 2 K/min as used in the calorimetry study.

3. Results

3.1. Microstructure and calorimetry tests

The sample x=0.32 is monoclinic M at room temperature, x=0.28 is rhombohedral R [5]. Figure 1 shows optical images of their microstructures.

The sample x=0.32, Fig. 1a,b, contains typical ~ 100 μm wide macrodomain plates [40]. Optical microscopy does not permit the observations of the internal microstructure of the macrodomains. Piezoelectric AFM defined this microstructure as $\langle 110 \rangle$ striations of submicron width [40].

The rhombohedral structure of x=0.28 is homogeneous on the macroscopic scale, Fig. 1 c. On the micron scale the microstructure is formed by clusters of ca. 10 μm elongation, 1 μm width twins aligned in two orthogonal <100> type directions. Similar twin microstructure has been reported by Bai et al. for the rhombohedral phase in a x=0.30 crystal [40]. The featureless light zones between the clusters likely contain polar nanoregions, revealed for x<0.30 by piezoelectric AFM [40].

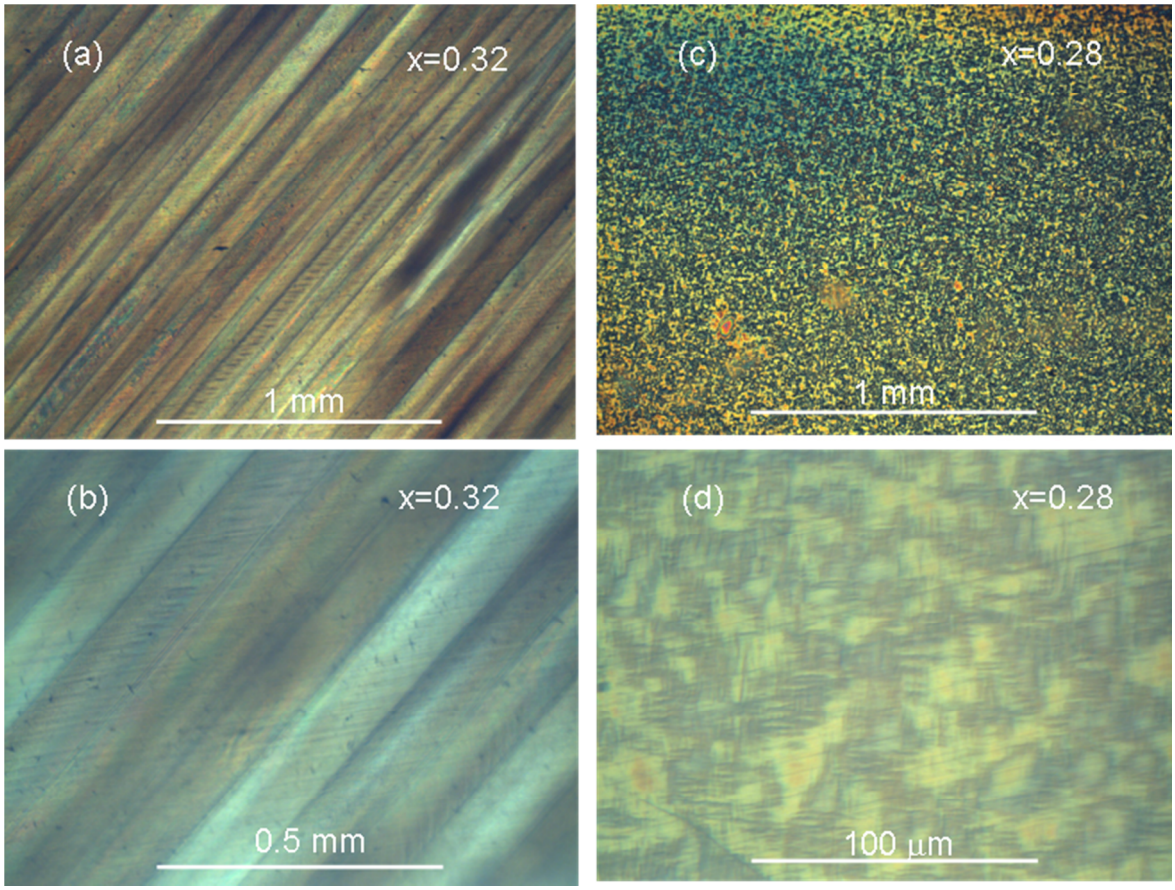

Figure 1. Polarized light optical images of the microstructure of (1-x)Pb($Mg_{1/3}Nb_{2/3}$)O_3-x$PbTiO_3$ crystals with x=0.32 (a,b) and x=0.28 (c,d).

The two pairs of heat flow peaks in Fig. 2a (x=0.32) indicate two first order transitions at 320-360 K and 400-420 K. The low- and high-temperature are the M↔T and T↔C transitions [5]. For the former, the peaks are at T_{H1}=352 K on heating and T_{C1}=338 K on cooling. The $T \leftrightarrow M$ phase transition thus shows a temperature hysteresis of ca. 14 K. The measured latent heats are 0.08 J/g on heating and 0.07 J/g on cooling. The transition appears more diffuse on cooling, making the determination of the latent heat less precise than on heating. The inset in Fig. 2a shows an example how the start and finish temperatures, 342 K and 332 K, were constructed using the tangent method for the cooling peak at T_{C1}=338 K. This example indicates that the start and finish temperatures of the transformation derived by tangent method underestimate the phase coexistence range. The $C \leftrightarrow T$ phase transition with T_{H2}=413 K on heating and T_{C2}=401 K on cooling is much less diffuse and is characterized by rather sharp peaks and a higher latent heat of 0.14 J/g both on cooling and heating. The transformation hysteresis of 12 K is comparable with the low-temperature transition.

Only one phase transition is measurable by DSC at x=0.28, Fig. 2b. A heat flow maximum is detected during heating at T_H=376 K with the latent heat of 0.05 J/g. The transition appears much more diffuse during cooling and only weak traces of the transition appear between 360 and 340 K (inset). For x=0.28 the DSC activity detected corresponds to the C↔R transition [5].

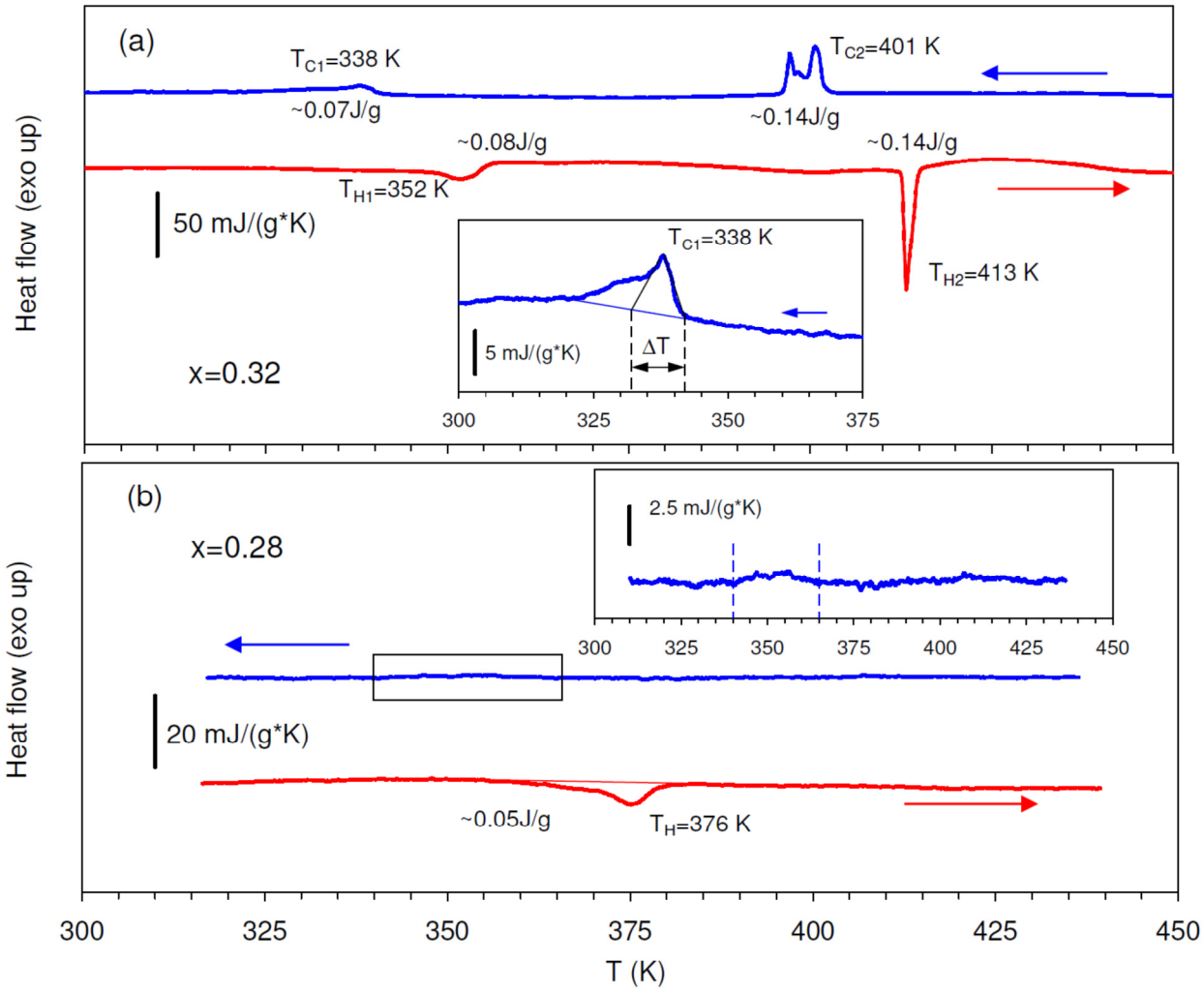

Figure 2. DSC scans for x=0.32 (a) and x=0.28 (b). The heat flow peak temperatures of the phase transitions on heating are denoted as T_{H1}, T_{H2} and on cooling T_{C1}, T_{C2} (a). The transition temperature T_H and the latent heat on heating are shown in (b). The inset in (b) shows a weak activity between 365 and 340 K on cooling.

3.2. Internal friction and Young´s modulus

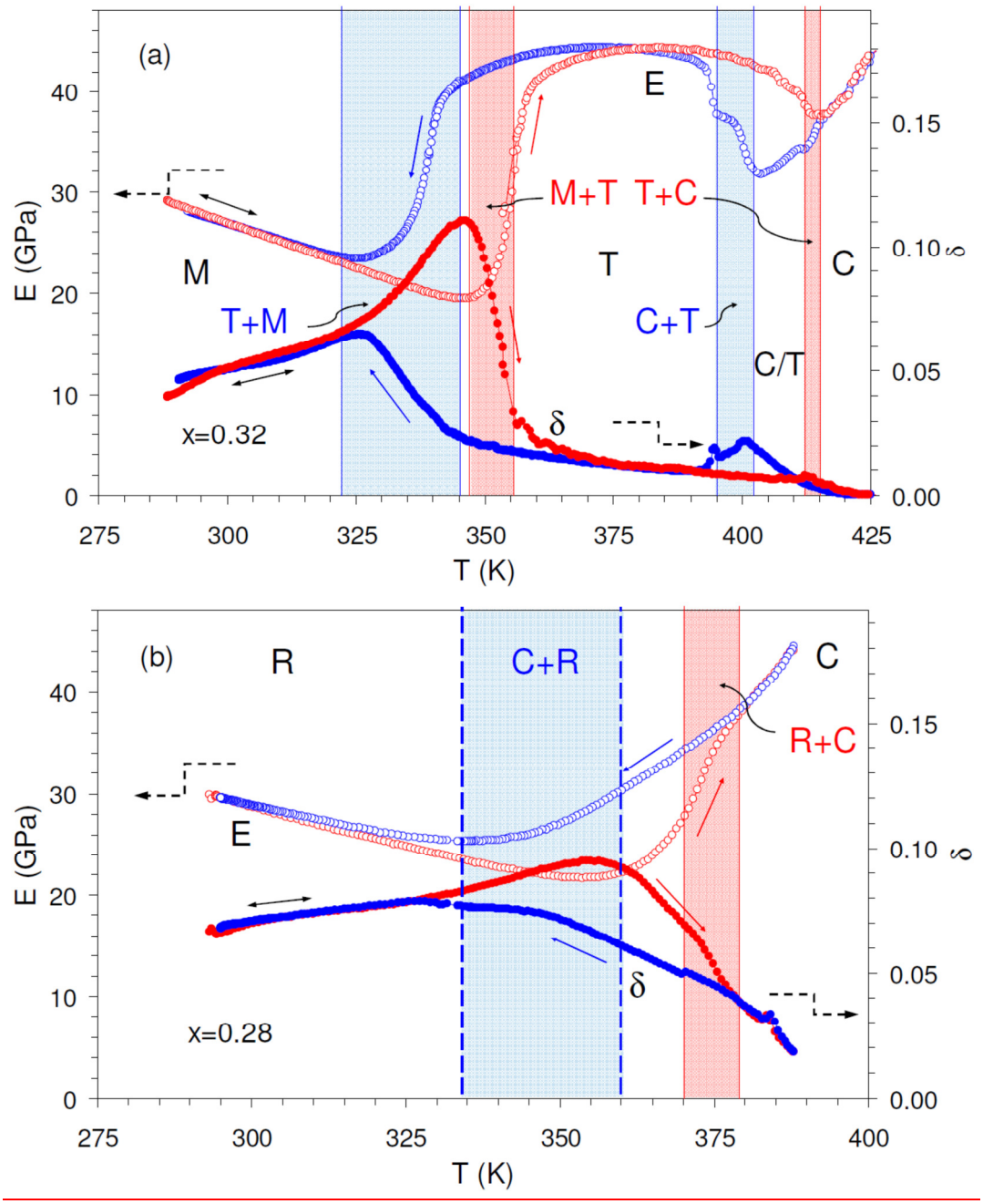

Figure 3. Temperature spectra of the Young´s modulus, E, and internal friction (logarithmic decrement δ) for x=0.32 (a) and x=0.28 (b) PMN-PT samples registered on heating (red symbols) and cooling (blue symbols). Heating/cooling rates are 2 K/min, the oscillatory strain amplitude is $\varepsilon_0 = 2\times10^{-7}$. Black letters C, T, M, R mark the regions of single cubic, tetragonal, monoclinic and rhombohedral phases. Red and blue vertical lines indicate the calorimetric temperatures of the start and finish of the $M \leftrightarrow T$, $T \leftrightarrow C$ and $C \leftrightarrow R$ transitions in Fig. 2. The regions between the blue vertical lines are two-phase regions on cooling (C+T, T+M for x=0.32 and C+R for x=0.28), between the red lines – two-phase regions on heating (M+T, T+C for x=0.32, R+C for x=0.28). The gap between the two-phase regions C/T (x=0.32) is monophase cubic on cooling and tetragonal on heating.

The temperature spectra of the Young´s modulus, E, and the internal friction, δ, for x=0.32 and x=0.28 are shown in Figure 3. Thin vertical lines in Fig. 3a and 3b mark the calorimetric start and finish temperatures for each phase transition. The coloured zones between vertical lines indicate two-phase fields: blue for cooling and red for heating. The two-phase region (x=0.28) on cooling is marked with broken lines since the determination of these temperatures from the DSC data is approximate and does not use the tangent method. The other calorimetric start and finish temperatures coincide rather well with the characteristic singularities of the Young´s modulus and internal friction behaviour. All data sets show thermal hysteresis, the thermal hysteresis of T↔C and M↔T transitions (x=0.32) is ca. 15 K
and ca. 20 K for R↔C (x=0.28). These values are consistent with the DSC data (x=0.32) and confirm that in x=0.28 the weak exothermal activity near 350 K during cooling is, indeed, associated with the diffuse C→R transition. The difference in the intensity of the R↔C transition during heating and cooling is confirmed by rapid and gradual modulus variations for the R→C and C→R transitions, Fig. 3b. Neither YM nor IF show thermal hysteresis in the single-phase regions, C, M, T for x=0.32 and C, R for x=0.28.
The YM shows characteristic softening in the cubic phase of both crystals. The onset of the C→T transition in x=0.32 coincides with the modulus minimum. The double DSC peak C→T (x=0.32) agrees with the two stages of the modulus increase and double internal friction peak, Fig. 3a. This confirms the correspondence between DSC and acoustic measurements. The M↔T transition in x=0.32 coincides with the abrupt modulus variation. The YM in the M phase is notably lower than in the tetragonal phase.

For x=0.28, the DSC data are less reliable, but a comparison of Fig. 2b and 3b indicates that the onset of the R→C transition can be located at the Young´s modulus minimum temperature near 360 K. It is indicative that the internal friction peak on heating is also located at this temperature. On cooling the x=0.28 sample, the minimum of the Young´s modulus and the internal friction peak are much less obvious due to the diffuseness of the phase transition. The behaviour of the modulus and internal friction is consistent with the absence of a clear DSC peak during the C→R transition. The two-phase fields for the $C \leftrightarrow R$ transitions (x=0.28) extend over an extremely wide temperature interval of 50 K, Fig. 3b.

In x=0.32 the two-phase fields are well separated for the $C \leftrightarrow T$ transition, whereas they are rather close for $T \leftrightarrow M$. The zones between the two-phase fields are single phase regions where different phases are found on heating and cooling. For the $C \leftrightarrow T$ this zone is marked in Fig. 3a by a multi-coloured symbol C/T. The existence of this temperature range is

also evident from the YM behaviour. The temperature coefficient $\frac{1}{E}\frac{\partial E}{\partial T}$ is positive on cooling, typical for softening of the cubic phase and negative on heating of the T phase. The tangent method applied to DSC data yields also a virtual C/R single phase region between the miscibility gaps C+R and R+C for the $C \leftrightarrow R$ transition, Fig. 3b. However, the tangent method underestimates the width of the miscibility gap. Figure 2b shows that this is true for the $C \rightarrow R$ transition and that on heating the two phases start to coexist already near 360 K. Therefore, the C/R region practically disappears in Fig. 3b, in contrast to C/T in x=0.32. This analysis of the virtual C/R region is consistent with the behaviour of the YM during heating for x=0.28, which starts to show on heating a positive temperature coefficient (i.e. the anomaly typical for the cubic phase) above ca. 360 K, Fig. 3b.

The common feature of both crystals is their extremely high IF value, up to $\delta \approx 0.1$ near the $T \leftrightarrow M$ transition (x=0.32) and close to R→C transition during heating (x=0.28). The IF remains high ($\delta \approx 0.05$) in the M and R phases. In contrast, the IF is relatively low ($\delta \approx 0.01$) in the tetragonal phase (x=0.32). The damping becomes very low in the cubic phase, above the temperatures of $T \rightarrow C$ and $R \rightarrow C$ transitions. These observations point to a high density of highly mobile lattice defects, like twin boundaries and/or other imperfections related to polar nanoregions, in the relaxor structure of x=0.28 and in the adaptive M state [1] of x=0.32.

Over the ranges $T \leftrightarrow M$ and $C \leftrightarrow R$, interphase boundaries might additionally contribute to increased damping.

The DSC and acoustic data indicate three categories of the temperature zones in the phase diagrams of x=0.28 and x=0.32 crystals close to the MPB:

1. True single-phase fields (C, T, M, R).
2. Single-phase fields in between the miscibility gaps where the phases are different on cooling and heating (C/T).
3. Two-phase fields, miscibility gaps with the coexistence of two phases (C+T, T+M, C+R); their positions are different for heating and cooling.

3.3. Dielectric parameters

We now discuss dielectric properties near the MPB [41].

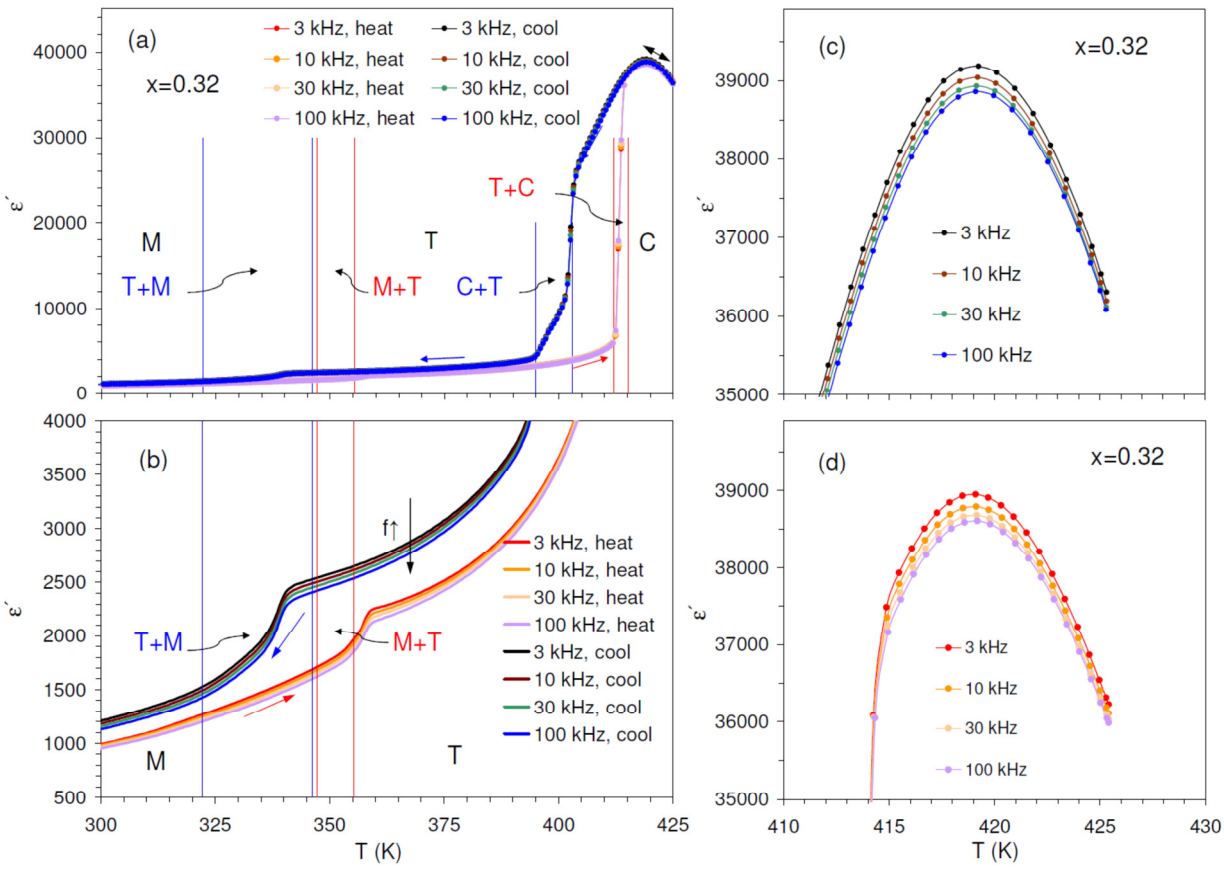

Figure 4. (a) Temperature spectra of the real part of the dielectric permittivity ε' for frequencies 3, 10, 30 and 100 kHz for cooling and heating scans of an unpoled x=0.32 PMN-PT sample.
Thin vertical lines mark the calorimetric start and finish temperatures of the cubic↔tetragonal and tetragonal↔monoclinic transitions on heating (red lines) and cooling (blue lines). The zones between the vertical lines are the two-phase regions of the cubic and tetragonal (C+T), tetragonal and monoclinic (T+M) phases on cooling (blue lines), and monoclinic and tetragonal (M+T), tetragonal and cubic (T+C) phases on heating (red lines); (b) details of the low-temperature part of the spectra on an expanded scale. Black letters M,T,C mark the single phase fields of the monoclinic, tetragonal and cubic phases.
(c), (d) details of the permittivity maximum during cooling (c) and heating (d).

Figures 4 and 5 show temperature spectra of the real component of the permittivity ε' and the loss tangent $\tan\delta = \frac{\varepsilon''}{\varepsilon'}$ for unpoled x=0.32. Figure 4a depicts the overall temperature spectra of ε' on heating and cooling. Figure 4b shows details of the ε' in the vicinity of the $T \leftrightarrow M$ transition. Thin vertical lines limit two-phase regions. Figure 4a shows that the $C \leftrightarrow T$ transition generates a significant change of ε' during cooling and heating. This transition is situated well below the T_m temperature of ε' maximum, which occurs in the cubic phase. ε' further decreases during the $T \rightarrow M$ transition (Fig. 4b). The temperature range of the $T \leftrightarrow M$

transition and its two-phase regions correspond with this decline on cooling and increase on heating. Figures 4c and 4d show that the shift of ε' maximum with frequency can be detected neither on cooling nor on heating, pointing to the absence of one of the hallmarks of the relaxor-type behaviour in x=0.32.

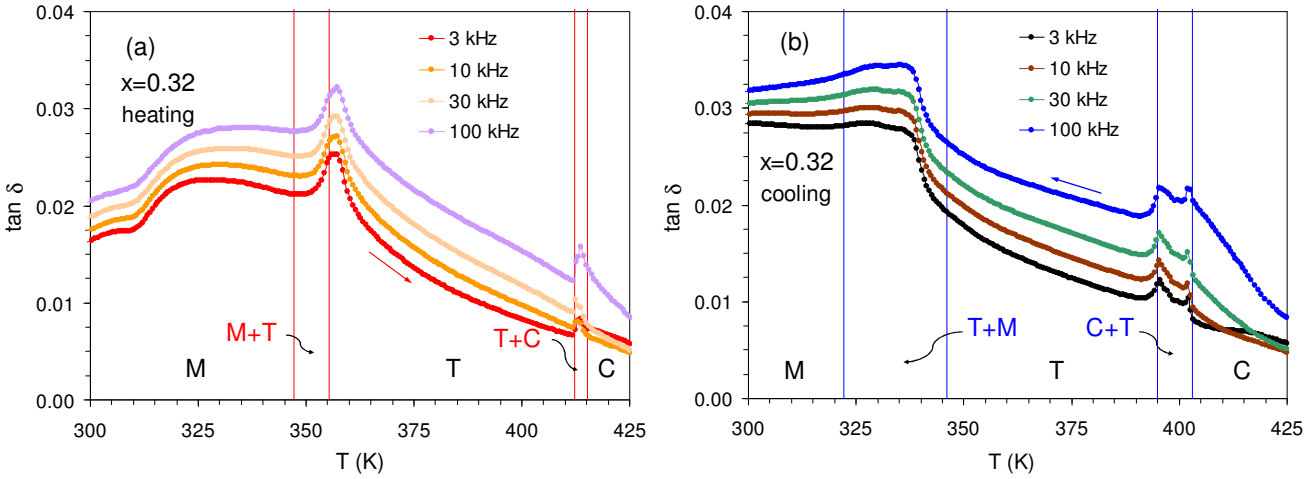

Figure 5. Temperature spectra of the loss tangent $\tan\delta$ at 3, 10, 30 and 100 kHz for an unpoled x=0.32 PMN-PT sample during (a) heating and (b) cooling. Thin vertical lines mark the calorimetric start and finish temperatures of the cubic↔tetragonal and tetragonal↔monoclinic transitions.

Figure 5 depicts temperature spectra of the loss tangent (x=0.32). The two-phase regions correlate with the dielectric loss maxima. The temperatures of $C \leftrightarrow T$ and $T \leftrightarrow M$ transitions do not show frequency dependence. The $C \rightarrow T$ dielectric loss peak, Fig. 5b, shows the same splitting as the DSC peak and the maximum of ultrasonic absorption, Figs. 2a, 3a.

Temperature spectra of ε' for x=0.28 crystal, Fig. 6, show much more gradual variations during the structural transitions than in x=0.32. Therefore, these transitions are difficult to analyse without supplementary DSC and acoustic data. A combination of the results obtained using three different techniques locates the limits of the two-phase regions on heating/cooling over the temperature ranges where thermal hysteresis of ε' disappears. As in the case of x=0.32 crystal, the transitions are substantially more diffuse on cooling than on heating.

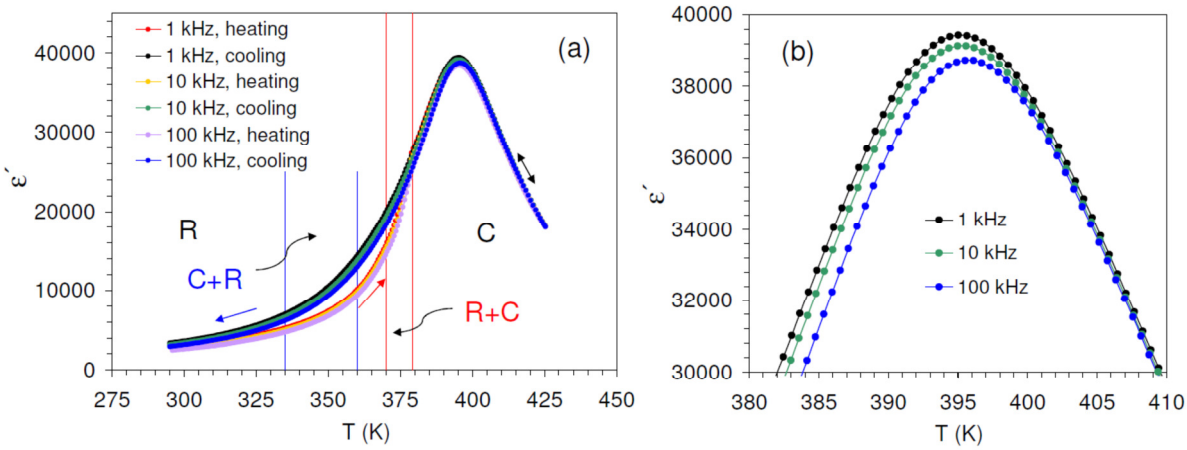

Figure 6. (a) Temperature spectra of the real part of the dielectric permittivity ε' for frequencies 1, 10 and 100 kHz for cooling and heating of an unpoled x=0.28 PMN-PT sample. Thin vertical lines mark the calorimetric start and finish temperatures of the rhombohedral-cubic transition on heating (red lines) and cubic-rhombohedral on cooling (blue lines). The zones between the vertical lines are the two-phase coexistence regions of cubic and rhombohedral (C+R) on cooling (blue lines) and rhombohedral and cubic phases (R+C) on heating (red lines). Black letters R and C mark the regions where only rhombohedral and cubic phases exist.
(b) details of the effect of frequency on the permittivity maximum during cooling.

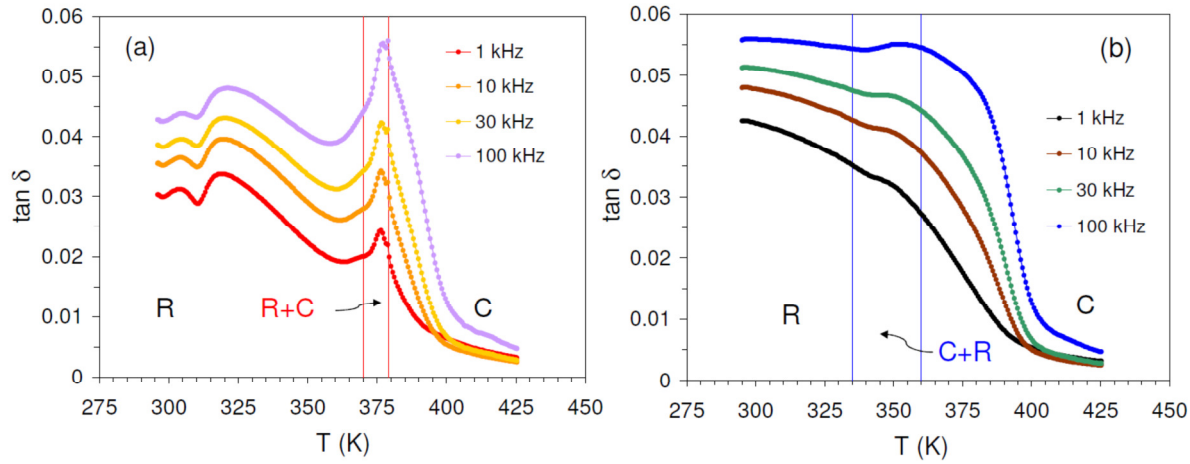

Figure 7. Temperature spectra of the loss tangent $\tan\delta$ for frequencies 1, 10, 30 and 100 kHz for an unpoled x=0.28 PMN-PT sample during (a) heating and (b) cooling. Thin vertical lines red in (a) and blue in (b) mark the calorimetric start and finish temperatures of the cubic↔tetragonal and tetragonal↔monoclinic transitions. They limit the two-phase regions (R+C) on heating (a) and (C+R) cooling (b).
Black letters R and C mark the regions where only rhombohedral and cubic phases exist.

Loss tangent data for x=0.28 crystal are shown in Fig. 7. In contrast to gradual ε' variation, dielectric losses peak more sharply on heating. The two-phase region (R+C) during the $R \rightarrow C$ transition, Fig. 7a, coincides with an abrupt increase of dielectric losses. Loss tangent declines rapidly in the cubic phase on further heating to ca. 400 K. The cooling scan, where the

localization of the $C \rightarrow R$ transition was difficult in DSC experiments, shows a gradual decline of losses over the two-phase (C+R) region, Fig. 7b, instead of sharp peak on heating, Fig. 7a.

Finally, Fig. 6b shows that for x=0.28, on the PMN-rich side of the phase diagram, a frequency shift of the ε' maximum is detected. However, the frequency shift is very small. The ratio $\frac{\Delta T_m}{T_m}\frac{1}{\Delta \log \omega}$ [42], with ω- angular frequency, is ca. 0.0003 per decade frequency, whereas this parameter calculated from the data for PMN [43] is ca. 0.03. Thus, a transition from relaxor to ferroelectric type of behaviour is practically completed on the PMN-rich side of the phase diagram.

4. Discussion

4.1. Transformation hysteresis, range, and phase diagram

The three experimental methods consistently classify all phase transitions as first order in our x=0.28 and x=0.32 PMN-PT single crystals. We take DSC data as a reference to determine the characteristic temperatures and temperature hysteresis of the transitions from the heat flow peaks. These characteristic temperatures are in good agreement with the ultrasonic and dielectric measurements.

Table 1 summarizes the temperatures of the DSC transformation peaks, the start and finish temperatures of the $C \leftrightarrow T$ and $T \leftrightarrow M$ transitions for x=0.32 and $C \leftrightarrow R$ transition for x=0.28. The estimated values of the latent heat are also shown. The evaluated latent heat of phase transitions between 0.05 and 0.14 J/g is typical for first order transitions in PMN and other ferroelastics [44-47].

Figure 8 shows the modified phase diagram for PMN-PT which takes into account the thermal hysteresis and the existence of two phase fields for $C \leftrightarrow R$, $C \leftrightarrow T$ and $T \leftrightarrow M$ transitions. We plot the limits of the two-phase regions in Fig. 8 as straight lines [5] and not as the predicted parabolic functions [2]. These straight lines converge near x=0.295. Our results are in excellent agreement with Noheda et al. [5] for the $T \leftrightarrow M$ transition. Their data correspond to the onset of the $M \rightarrow T$ transition [5] and coincide with the position of the low-temperature limit of our two-phase field M+T on heating.

Table 1. Start (T_s), peak (T_p) and finish (T_f) temperatures, two-phase fields ($|T_s - T_f|$) and latent heats Q of the $C \rightarrow T$, $T \rightarrow M$ structural transitions on cooling and $M \rightarrow T$, $T \rightarrow C$ and $R \rightarrow C$ transitions on heating in (1-x)Pb($Mg_{1/3}Nb_{2/3}$)O_3-x$PbTiO_3$

Crystal	*Transition*	T_s *(K)*	T_p *(K)*	T_f *(K)*	$\|T_s - T_f\|$ *(K)*	*Q (J/g)*
x=0.32	$C \rightarrow T$	402	399*	396	6	0.14
	$T \rightarrow M$	342	338	332	10	0.07
	$M \rightarrow T$	347	352	356	9	0.08
	$T \rightarrow C$	412	413	415	3	0.14
x=0.28	$C \rightarrow R$	365**	355**	340**	25	
	$R \rightarrow C$	370	376	379	9	0.05

*average value of the temperatures of two DSC peaks
**approximate values obtained without using tangent method

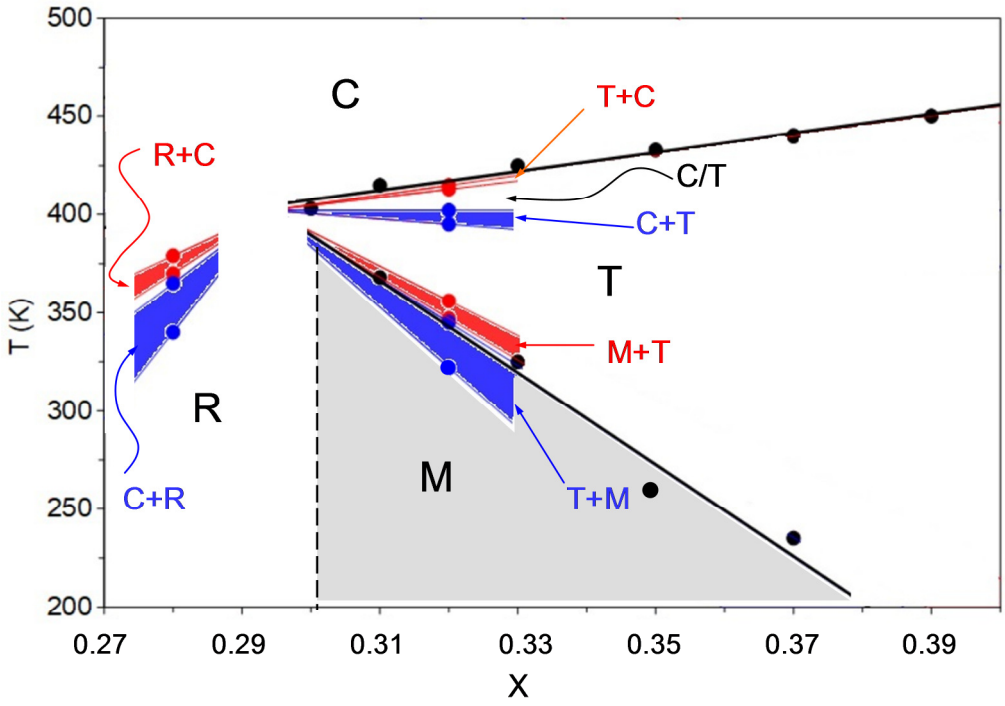

Figure 8. Phase diagram of the (1-x)Pb($Mg_{1/3}Nb_{2/3}$)O_3-x$PbTiO_3$ system close to the MPB including thermal hysteresis and three types of the regions for weakly first order transitions $C \leftrightarrow R$, $C \leftrightarrow T$ and $T \leftrightarrow M$

- single phase regions C, T, M and R,
- single phase region C/T wherein the phase is different on cooling (C) and heating (T),
- miscibility gaps (two phase fields on cooling C+T, T+M, C+R and on heating T+C, M+T, R+C).

Black points are from Noheda et al. [5]. The blue regions mark two phase fields on cooling, the red fields on heating. The start and finish temperatures of all transitions (except for the $C \rightarrow R$ on cooling) are determined from calorimetry.

The phase diagram can be summarized as follows:

- The $C \leftrightarrow R$ and $C \leftrightarrow T$ transition are (weakly) first order. The tricritical points may be located even closer to the MPB line, between x=0.28 and x=0.32 (they may not exist at all). The observation of a first order transition under zero field in PMN-PT with x=0.295 [47] cast further doubts into the existence of tricritical points in PMN-PT. The transitory IF patterns were reported for PZT very close to the MPB [6,15-17], pointing to a typical first order transition. As a consequence, the hypothetical tricritical points [2,5] may exist neither in PMN-PT nor in PZT.
- The two-phase fields do not overlap in our experimental data and form 6 more ($C \leftrightarrow T$) or less ($C \leftrightarrow R$, $T \leftrightarrow M$) separate zones in the phase diagram. The overlap of the two-phase fields could be expected closer to the MPB. New single-phase regions may appear in the phase diagram in between the two-phase fields on cooling and heating instead of overlapping phase regions. In these regions, the phases are different on cooling and heating. The existence of this region is exemplified by the $C \leftrightarrow T$ transition in x=0.32. In this region, denoted C/T, Fig. 8, the single cubic phase exists on cooling and single tetragonal phase on heating.
- The two-phase fields for $C \leftrightarrow R$ transition in x=0.28 and $T \leftrightarrow M$ in x=0.32 extend over a temperature window of ca. 50 K, notably wider than for the $C \leftrightarrow T$ transition in x=0.32. This difference correlates with the higher latent heat for the $C \leftrightarrow T$ transition in x=0.32.

The phenomenological crystallographic theory of ferroelastic martensitic transformations [48,49] was successfully applied to describe twinning and habit plane orientation during $C \leftrightarrow T$ transition in $PbTiO_3$ single crystals despite strong polarity of $PbTiO_3$ and concerns related to the possible effects of stored electric energy [50]. The concept of the martensitic transformation was used to interpret the transition between polar nanoregion and ferroelectric states of the relaxor-ferroelectric $Pb(Zn_{1/3}Nb_{2/3})O_3$-$PbLa(ZrTi)O_3$ solid solution [51]. Below we use a conventional thermodynamic description for the properties of the temperature hysteresis and two phase regions during $C \leftrightarrow R$ (x=0.28) and $T \leftrightarrow M$, $C \leftrightarrow T$ (x=0.32) transitions. We refer to the total energy stored during transitions in PMN-PT on cooling as "elastic stored energy". We assume that the stored energy is fully recovered during the corresponding transformations on heating.

The $C \leftrightarrow R$ and $T \leftrightarrow M$ transitions, compared with $C \leftrightarrow T$, are characterized by: (i) a wider temperature hysteresis; (ii) adjacent two phase ranges not separated by a single C/R and T/M fields; (iii) a more diffuse transition on cooling than on heating; and (iv) a lower latent

heat, Table 1. These characteristics can be interpreted qualitatively using thermodynamic analysis of ferroelastic transitions [52]. The heat flow in the DSC test is proportional to the variation of the volume fraction of the low-temperature phase F, $\frac{\partial Q}{\partial T} \propto \frac{\partial F}{\partial T}$, if the volume (density) change during the transition is neglected. The integration of the normalized heat flow for $C \leftrightarrow T$ and $T \leftrightarrow M$ transitions yields then the volume fraction F which is shown in Fig. 9a,c. Vertical dotted lines mark the positions of the start and the finish temperatures on cooling, C_s,C_f , and on heating, H_s, H_f , derived from the tangent method. The patterns of *F(T)* comply with the features (i)-(iii) of the heat flow data. The black curve in Fig. 9c represents the $R \rightarrow C$ transition on heating for x=0.28. Figures 9b,d show schematically two typical *F(T)* patterns for the first order ferroelastic transition [53,54] which agree with the experimental observations in Fig. 9a,c. *F(T)* in Fig. 9b,d implies that (i) a multivariant structure is formed that stores elastic energy and (ii) the motion of phase boundaries against constant friction stresses during the transition produces frictional work [52,53]. The width of the two-phase regions, C_s-C_f and H_f-H_s, is then determined by the elastic stored energy of the polyvariant structure, whereas the hysteresis of the transformation relates to friction during the motion of interfaces during the transition [52-54]. Figure 9b represents the case of relatively high friction and low stored energy that features narrow miscibility gaps. A combination of the narrow two-phase regions and relatively wide hysteresis creates a wide temperature range, H_s-C_s, wherein different single phases exist on cooling and on heating.

This effect is known in martensitic alloys. For instance, $H_s - C_s > 0$ in Ni-Mn-Ga single crystals [55] Wollants et al. assumed that for a typical "hypothetical shape memory alloy" $H_s - C_s = 15K$ [52]. In perovskites, Lee et al. [56] observed that $H_S \approx C_S$ for a nearly stoichiometric $BaTiO_3$ [56] and considered this as the equilibrium temperature. We note that thermodynamics requires $H_s > C_f$ for a martensitic transformation and permits both $H_s > C_s$ and $H_s < C_s$, whereas a reasonable approximation of the equilibrium temperature for multiple interface transformation is given by $T_0 = (C_s + H_f)/2$ [57]. During a single crystal-single interface transition the *F(T)* trajectory becomes nearly rectangular due to the absence of elastic stored energy [54,57]. The agreement between Figs. 9b and 9a allows us to ascribe these features to the $C \leftrightarrow T$ transition.

Figure 9d corresponds to the inverse situation of a relatively high elastic stored energy. The width of the transformation ranges C_s-C_f and H_f-H_s is greater than in Fig. 9b, and the miscibility gaps on cooling and heating join, $C_s \approx H_s$. A single-phase regime with different

phases on cooling and heating does not exist, therefore. The dashed line in Fig. 9d indicates *F(T)* on cooling when the friction stress increases with *F*, provoking a more diffuse transition on cooling then on heating. The schematic pattern of Fig. 9d fits the experimental data for the $T \leftrightarrow M$ transition, Fig. 9c. The same analysis can be done for x=0.28 only on heating, Fig. 9c, since the DSC data are unreliable on cooling. However, wide hysteresis and wide two-phase region on heating - the main features of the $C \leftrightarrow R$ transition - are the same as in $T \leftrightarrow M$. Hence, the difference in the patterns of $C \leftrightarrow T$ and of $C \leftrightarrow R$ and $T \leftrightarrow M$ transitions can be qualitatively interpreted in terms of friction during the motion of interfaces and elastic energy stored during the transition. Friction is relatively high in the $C \leftrightarrow T$ transition, elastic energy is high in $C \leftrightarrow R$ and $T \leftrightarrow M$.

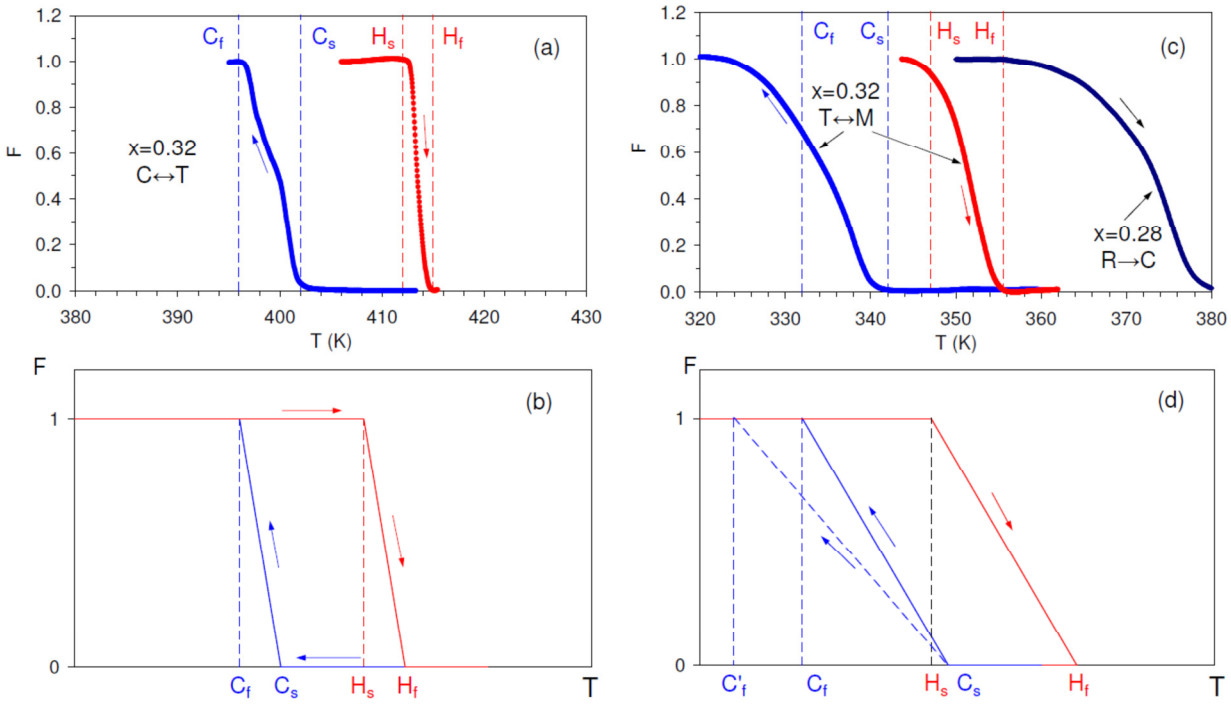

Figure 9.
(a,c) Experimental temperature dependences of the fraction of the low-temperature phase, F, for the C↔T (a) and T↔M (c) transitions in x=0.32 PMN-PT single crystal; C_s, C_f and H_s, H_f are the start and finish temperatures on cooling and heating. The black curve in (c) is the F(T) dependence for R→C transition on heating in x=0.28 crystal.
(b,d) Adapted from [53]: schematic representation of F versus T during a first order ferroelastic multiple variant transition on cooling (blue lines) and heating (red lines);solid lines are the F(T) trajectories when the same constant friction force acts on interphase boundaries during cooling and heating, dashed line in (d) is F(T) trajectory when friction stress increases on cooling with the amount of transformed material; (b) relatively low elastic energy stored/released; (d) relatively high elastic energy.
The last assumption is consistent with the observed microstructures, Fig. 1. The T phase is formed by 100 micron wide parallel twins that easily accommodate the transformation strain.

The twin structure of the x=0.28 crystal consists of patches of orthogonal micron-size twins that should create high stresses. The lower elastic energy for the $C \leftrightarrow T$ transition does not contradict its higher latent heat compared with $C \leftrightarrow R$ and $T \leftrightarrow M$ since the elastic energy decreases the latent heats of the transition during cooling and heating, Q_c and Q_h [52]:

$$\begin{aligned} -Q_c &= -\Delta H_{ch}^{p\to f} + E_{st}^{p\to f} \\ Q_h &= \Delta H_{ch}^{f\to p} - E_{st}^{f\to p} \end{aligned}, \qquad (4)$$

where $\Delta H_{ch}^{p\to f}$ and $\Delta H_{ch}^{f\to p}$ are chemical enthalpy changes during the para- to ferroelastic and ferro- to paraelastic transitions; $E_{st}^{p\to f}$ and $E_{st}^{f\to p}$ are the stored elastic energies.

Similar to the present results, the $T \to C$ transition was very sharp, whereas $R \to T$ was very diffuse for several PZT compositions close to the MPB [15-17].

4.2. Athermal versus iso/anisothermal transition in PMN-PT

Different regions in the phase diagram of Fig. 8 were identified under a cooling/heating rate of 2K/min. The question then is whether the hysteresis and two-phase fields are rate-independent or rate dependent on the laboratory time scale. This would imply that the transitions in PMN-PT are either athermal (when the thermal activation is irrelevant) or iso-/anisothermal (thermal activation is involved in the transition) [58-60]. In the former case the transition thermal hysteresis is a sequence of metastable states, in the latter – the system is allowed to relax to the state of minimum energy and the hysteresis might vanish eventually.

The excellent coincidence between the low temperature limit of the two-phase field M+T in Fig. 8 with corresponding isothermal data points by Noheda et al. [5] appear to point to a time-independent (M+T) field (x=0.32). In ferroelastic Ni-Ti system with a number of structural transitions, those with higher thermal hysteresis (B2→B19´transition) or wider two-phase field (more diffuse B19→B19´ transformation) are more prone to be affected by thermal activation [60]. More diffuse $C \leftrightarrow R$ transition (x=0.28), therefore, can demonstrate rate dependence due to thermal activation involved. We now use non-linear acoustic effects, exclusively related to moving twins in PMN-PT, as indicator for the stability with time of the twin structure and, hence, for the fraction of the rhombohedral phase.

The strain amplitude dependence in Fig.10a allows us to select the low- and high strain amplitudes for simultaneous measurements of linear and non-linear IF versus temperature and time as $\varepsilon_0^{low}=5\times10^{-7}$ and $\varepsilon_0^{high}=4\times10^{-5}$. We assume [61] additivity of linear and non-linear terms. Temperature spectra of the linear and non-linear IF components for x=0.28 in Fig. 10b indicate that the $C \leftrightarrow R$ transition is marked by δ_h maxima both on cooling and heating, qualitatively like those of the linear term δ_i. Several cooling scans were interrupted at 350, 330 and 310 K to observe the isothermal kinetics of δ_h. The first temperature (350 K) belongs to the two phase C+R region, the last two (330 and 310 K) fall within the single R-phase field. The results shown in Fig. 11a indicate isothermal decrease of δ_h in the R phase, which is related to the relaxation of the complex R phase structure (Fig. 1). The data do not follow

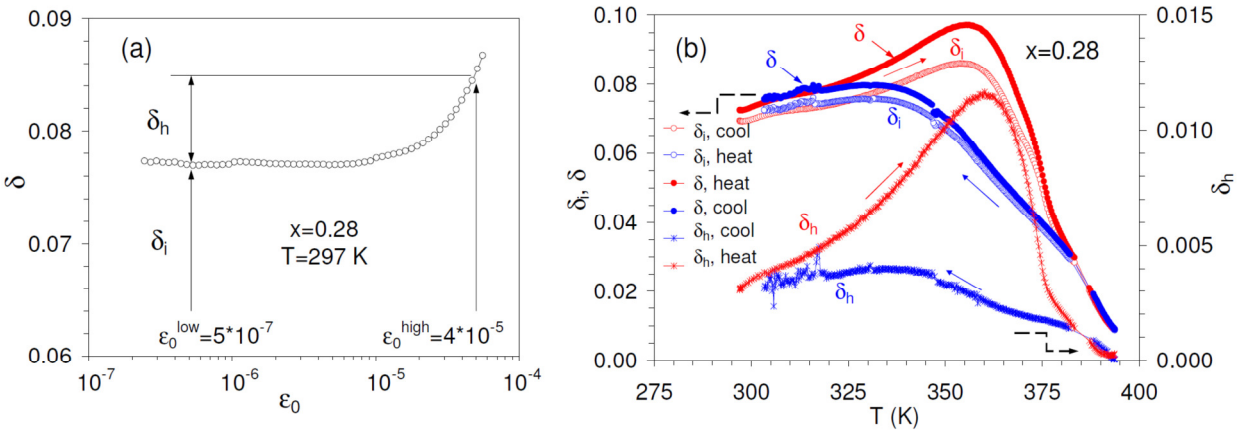

Figure 10.

(a) Strain amplitude dependence of the internal friction at room temperature for the x=0.28 sample. Separation of linear δ_i and non-linear δ_h internal friction terms is shown; strain amplitudes ε_0^{low} and ε_0^{high} are those chosen for the measurements of the temperature spectra of linear and non-linear damping terms (shown in panel (b));

(b) temperature spectra of the linear δ_i , the total δ and non-linear δ_h internal friction components for x=0.28 crystal; the linear spectra is registered at a low strain amplitude $\varepsilon_0^{low}=5\times10^{-7}$, the total internal friction is measured at high strain amplitude $\varepsilon_0^{high}=4\times10^{-5}$, the non-linear term is the difference between the spectra at high and low strain amplitude, $\varepsilon_0^{high}=4\times10^{-5}$ and $\varepsilon_0^{low}=5\times10^{-7}$, respectively.

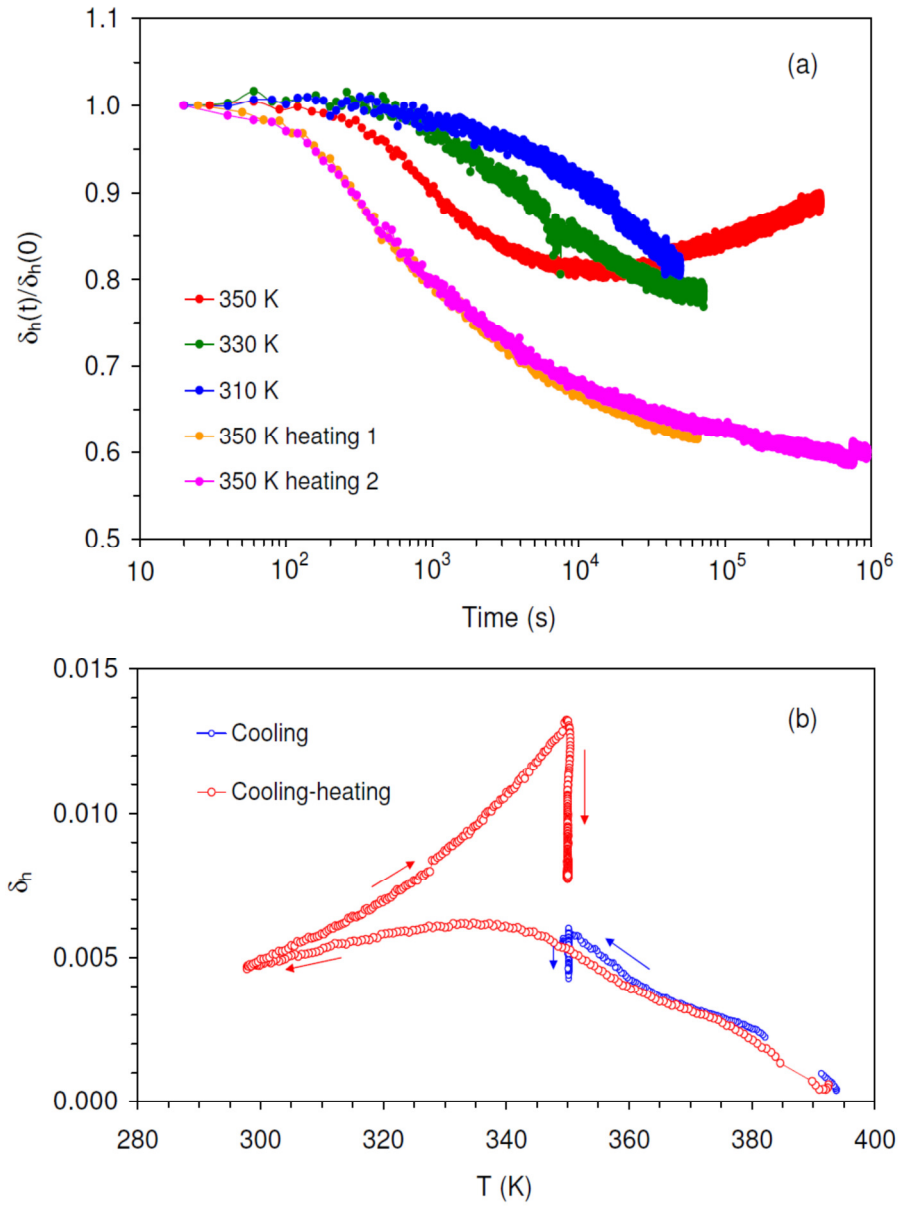

Figure 11. (a) Kinetics of isothermal relaxation of the normalized non-linear internal friction component δ_h during isothermal holdings at 350, 330, 310 K on cooling and 350 K on heating. The results of two relaxations at 350 K after interruption of heating are shown with the duration of 24 hrs and 14 days.
(b) Temperature spectra of the non-linear internal friction term δ_h on cooling (blue symbols) and on cooling with subsequent heating (red symbols); vertical arrows mark interruptions of temperature scans and isothermal holdings on cooling and heating at 350 K.

simple exponential or logarithmic kinetics. Therefore, in terms of the activation energies, neither of the two extreme cases, namely a single value or their flat distribution, account for the observed kinetics. Data in Fig. 11a include a substantial incubation time, increasing with lowering temperature. Hence, application of the Kohlrausch-Watts-Williams stretched exponent [62] implies a significant error for low waiting times. Therefore, treatment of the

experimental data in Fig. 11a requires other approaches. If the cooling is interrupted in the (C+R) field at 350 K, the isothermal variation of δ_h is non-monotonous: the initial decline up to 20×10^4 s is followed by a gradual increase that does not saturate after more than a week of isothermal measurements. Thus, the δ_h kinetics in the two-phase C+R field on cooling is a superposition of two opposite trends: a conventional relaxation as in single phase R field and a more long-term δ_h increase, which reflects the isothermal progression of the C→R transition, Fig. 10b. Thus, the diffuse C→R transition (x=0.28) should be classified as an isothermal or anisothermal [58,59] structural transition. Unfortunately, the method employed is not applicable to the R→C transition on heating, since both relaxation and isothermal accumulation of the cubic phase reduce δ_h. Nevertheless, the isothermal kinetics was registered at 350 K after interruption of heating in order to compare the relaxed δ_h values after relaxations on cooling and heating. This experiment is a check whether the cooling and heating relaxations yield the collapse of δ_h values. Figure 11a shows that after interruption of heating at 350 K the kinetics of the monotonous δ_h decline becomes very slow. Figure 11b shows the δ_h temperature spectra together with the 350 K isothermal relaxations on cooling and heating. These results confirm that the "dynamic" difference between δ_h values during continuous cooling and heating scans reduces strongly for final isothermal points. Nevertheless, the final points after relaxations for ca. 10^6 s do not collapse. Thus, the thermal hysteresis persists for relaxation times orders of magnitude longer than the typical laboratory time scale used in structural characterization of PMN-PT (X ray, neutron scattering, acoustic, DSC tests, etc.). More experiments and different techniques are needed to verify the athermal or isothermal nature of other structural transitions in PMN-PT.

5. Conclusions

1. Under dynamic conditions (continuous cooling-heating scans), all phase transitions in (1-x)$Pb(Mg_{1/3}Nb_{2/3})O_3$-x$PbTiO_3$ single crystals close to the morphotropic phase boundary with x =0.28 and x=0.32 ($C \leftrightarrow T$ and $T \leftrightarrow M$ in x=0.32 and $C \leftrightarrow R$ in x=0.28) are classified as the first order ones with corresponding values of heat effect, thermal hysteresis and two phase regions. The tricritical points, if they exist in PMN-PT, should be located in between the compositions studied, x=0.28 and x=0.32, very close to morphotropic phase boundary;

2. Modified phase diagram close to the MPB of the PMN-PT system is suggested that is composed of three categories of fields:

- True single phase fields, representing the cubic (C), rhombohedral (R), tetragonal (T) and monoclinic (M) phases
- Single phase field wherein the type of the phase is different on cooling and heating, C/T field in x=0.32;
- Two-phase fields where the two phases coexist, C+R, C+T, T+M;

3. Although the phase diagram obtained is dynamic and non-equilibrium, corresponding to continuous cooling-heating scans, the relaxations orders of magnitude longer than the characteristic laboratory time scale confirm the existence of thermal hysteresis;

4. The differences in the width of the two-phase fields and in thermal hysteresis for $C \leftrightarrow R$, $T \leftrightarrow M$ and $C \leftrightarrow T$ transitions are interpreted qualitatively using a thermodynamic description of the ferroelastic transitions;

5. At least some transitions (e.g. cubic-rhombohedral on cooling for x=0.28) show long-term gradual accumulation of the product phase at constant temperature and are classified as isothermal or anisothermal. The accumulation of the ferroelastic phase at constant temperature introduces time as an additional variable in structural characterization of PMN-PT.

Acknowledgements

The work was supported by MCIN/AEI/10.13039/501100011033 and "FEDER Una manera de hacer Europa, EU", project RTI2018-094683-B-C51.

X. Wang acknowledges the financial support from the National Nature Science Foundation of China (No. 51905310). EKHS is grateful to EPSRC for support (EP/P024904/1) and the EU´s Horizon 2020 programme under the Marie Sklodowska-Curie Grant (861153).

References

1. D. D. Viehland, E.K.H. Salje, Domain boundary dominated systems: adaptive structures and functional twin boundaries, Adv. Phys. 63:4 (2014) 267-326.

2. G. A. Rossetti Jr., A.G. Khachaturyan, G. Akcay, Y. Ni, Ferroelectric solid solutions with morphotropic boundaries: Vanishing polarization anisotropy, adaptive, polar glass, and two-phase states, J. Appl. Phys. 103 (2008) 114113.

3. H. Cao, J.F. Li, D. Viehland, G. Xu, Fragile phase stability in $(1-x)Pb(Mg_{1/3}Nb_{2/3})O_3$-$xPbTiO_3$ crystals: A comparison of [001] and [110] field-cooled phase diagrams, Phys. Rev. B 73 (2006) 184110.

4. V.V. Eremkin, V.G. Smotrakov, E.G. Fesenko, Structural phase transitions in $PbZr_{1-x}Ti_xO_3$ crystals, Ferroelectrics, 110 (1990) 137-144.

5. B. Noheda, D.E. Cox, G. Shirane, J. Gao, Z.-G. Ye, Phase diagram of the ferroelectric relaxor $(1-x)Pb(Mg_{1/3}Nb_{2/3})O_3$-$xPbTiO_3$, Phys. Rev. B. 66 (2002) 054104.

6. A. Bouzid, E.M. Bourim, M. Gabbay, G. Fantozzi, PZT phase diagram determination by measurement of elastic moduli, J. Eur. Cer. Soc. 25 (2005) 3213-3221.

7. A. K. Singh, D. Pandey, O. Zaharko, Powder neutron diffraction study of phase transitions in and a phase diagram of $(1-x)[Pb(Mg_{1/3}Nb_{2/3})]O_3$-$xPbTiO_3$, Phys. Rev. B 74 (2006) 024101.

8. F. Cordero, Elastic properties and enhanced piezoelectric response at morphotropic phase boundary, Materials 8 (2015) 8195-8245.

9. Y. Song, X. Chen, V. Dabade, T.W. Shield, R. D. James, Enhanced reversibility and unusual microstructure of a phase-transforming material, Nature 502 (2013) 85-88.

10. F. Zhuo, D. Damjanovic, Q. Li, Y. Zhou,Y. Ji, Q. Yan, Y. Zhang, Y. Zhou, X. Chu, Giant shape memory and domain memory effects in antiferroelectric single crystals, Mater. Horizons, 6 (2019) 1699-1706.

11. K. Otsuka, C.M. Waymen, Chapter 1 in: Shape memory materials, K. Otsuka, C.M. Wayman, Eds., Cambridge Univ. Press, 1998.

12. B. Noheda, J.A. Gonzalo, L.E. Cross, RR. Guo, S.-E. Park, D.E. Cox, G. Shirane, Tetragonal-to-monoclinic phase transition in a ferroelectric perovskite: The structure of $PbZr_{0.52}Ti_{0.48}O_3$, Phys. Rev. B 61 (2000) 8687-8695.

13. D. Pandey, A.K. Singh, S. Baik, Stability of ferroic phases in the highly piezoelectric $Pb(Zr_xTi_{1-x})O_3$ ceramics, Acta Crystallographica Sect. A, Foundations of Crystallography, A64 (2008) 192-203.

14. D. La-Orauttapong, B. Noheda, Z.-G. Ye, P. M. Gehring, J. Toulouse, D. E. Cox, G. Shirane, Phase diagram of the relaxor ferroelectric (1-x)$Pb(Zn_{1/3}Nb_{2/3})O_3$-x$PbTiO_3$, Phys. Rev. B 65 (2002) 144101.

15. E. Bourim, H. Idrissi, B. Cheng, M. Gabbay, G. Fantozzi, Elastic modulus and mechanical loss associated with phase transition and domain wall motion in PZT based ceramics, Journ. de Phys. IV Proceedings, EDP Sciences, 1996, 06 (C8), C8-633-C8-636.

16. G. Fantozzi, Chapter 5.2. Ferroelectricity, Mater. Science Forum, 366-368 (2001) 361-381.

17. E.M. Bourim, H. Tanaka, M. Gabbay, G. Fantozzi, Internal friction and dielectric measurements in lead zirconate titanate ferroelectric ceramics, Jpn. J. Appl. Phys. 39 (2000) 5542-5547.

18. P. Bao, F. Yan, W. Li, Y.R. Dai, H.M. Shen, J.S. Zhu, Y.N. Wang, H. Chan, C.-L. Choi, Mechanical properties related to the relaxor-ferroelectric phase transition of titanium-doped lead magnesium niobate, Appl. Phys. Lett. 81 (2002) 2059-2061.

19. Ragini, S. K. Mishra, D. Pandey, H. Lemmens, G. Van Tendeloo, Evidence for another low-temperature phase transition in tetragonal $Pb(Zr_xTi_{1-x})O_3$ (x=0.515,0.520), Phys. Rev. B 64 (2001) 054101.

20. M. Algueró, B. Jimenez, L. Pardo, Rayleigh type behaviour of the Young´s modulus of unpoled ferroelectric ceramics and its dependence on temperature, Appl. Phys. Lett. 83 (2003) 2641-2643.

21. Y.R. Dai, P. Bao, H.M. Shen, D. Su, J.S. Ju, Y.N. Wang, Y.P. Zhu, Internal friction study on low-temperature phase transitions in lead zirconate titanite ferroelectric ceramics, Appl. Phys. Lett. 82 (2003) 109-111.

22. F. Li, S. Zhang, Z. Xu, X. Wei, J. Luo, T.R. Shrout, Composition and phase dependence of the intrinsic and extrinsic piezoelectric activity of domain engineered (1-x)$Pb(Mg_{1/3}Nb_{2/3})O_3$-x$PbTiO_3$ crystals, J. Appl. Phys. 108 (2010) 034106.

23. G. A. Rossetti, A. Navrotsky, Calorimetric investigation of tricritical behavior in tetragonal $Pb(Zr_xTi_{1-x})O3$, J. Sol. State Chem. 144 (1999) 188-194.

24. R. S. Solanki, S.K. Mishra, Y. Kuroiwa, C. Moriyoshi, D. Pandey, Evidence for a tricritical point coinciding with the triple point in $(Pb_{0.94}Sr_{0.06})(Zr_xTi_{1-x})O_3$: A combined synchrotron x-ray diffraction, dielectric and Landau theory study, Phys. Rev. B 88 (2013) 184109.

25. B. Noheda, N. Cereceda, T. Iglesias, G. Lifante, J.A. Gonzalo, H.T. Chen, Y.L. Wang, Composition dependence of the ferroelectric-paraelectric transition in the mixed system $PbZr_{1-x}Ti_xO3$, Phys. Rev. B 51 (1995) 16388-16391.

26. S . K. Mishra, P. Singh, D. Pandey, Thermodynamic nature of phase transitions in $Pb(Zr_xTi_{1-x})O_3$ ceramics near the morphotropic phase boundary. I. Structural studies, Phil. Mag. B 76 (1997) 213-226.

27. S. K. Mishra, D. Pandey, Thermodynamic nature of phase transitions in $Pb(Zr_xTi_{1-x})O_3$ ceramics near the morphotropic phase boundary. II. Dielectric and piezoelectric studies, Phil. Mag. B 76 (1997) 227-240.

28. A.K. Singh, D. Pandey, Evidence for M_B and M_C phases in the morphotropic phase boundary region of $(1-x)Pb(Mg_{1/3}Nb_{2/3})O_3$-$xPbTiO_3$: A Rietveld study, Phys. Rev. B 67 (2003) 064102.

29. M.-S. Yoon, H.M. Jang, Relaxor-normal ferroelectric transition in tetragonal-rich field of $Pb(Ni_{1/3}Nb_{2/3})O_3$-$PbTiO_3$-$PbZrO_3$ system, J. Appl. Phys. 77(1995) 3991-4001.

30. J. San Juan, R.B. Pérez-Sáez, Chapter 5.4. Transitory effects, Mater. Science Forum 366-368 (2001) 416-436.

31. S. Kustov, A. Saren, B. D'Agosto, K. Sapozhnikov, V. Nikolaev, K. Ullakko, Transitory ultrasonic absorption in "Domain Engineered" structures of 10M Ni-Mn-Ga martensite, Metals 11 (2021) 1505.

32. F. Cordero, F. Craciun, C. Galassi, Low-temperature phase transformations of $PbZr_{1-x}Ti_xO_3$ in the morphotropic phase-boundary región, Phys. Rev. Lett. 98 (2007) 255701.

33. M. Algueró, B. Jimenez, L. Pardo, Transition between the relaxor and ferroelectric states for $(1-x)Pb(Mg_{1/3}Nb_{2/3})O_3$-$xPbTiO_3$ with x=0.2 and 0.3 policrystalline aggregates, Appl. Phys. Lett. 87 (2005) 082910.

34. Y. Yu, X.-S. Wang, H. Zou, Y-X. Li, X. Yao, Polarization effect for dielectric and mechanical behaviours in $Pb(Mg_{1/3}Nb_{2/3})_{0.71}Ti_{0.29}O_3$ crystal, Mater. Res. Bull. 69 (2015) 56-67.

35. W.H. Robinson, A. Edgar, The Piezoelectric Method of Determining Mechanical Damping at Frequencies of 30 to 200 KHz, IEEE Trans. Sonics Ultrasonics 21 (1974) 98-105.

36. G. Gremaud, S. Kustov, O. Bremnes, Ultrasonic techniques: PUCOT and ACT, Mater. Sci. Forum 366-368 (2001) 652-666.

37. S. Kustov, S. Golyandin, A. Ichino, G. Gremaud, A New Design of Automated Piezoelectric Composite Oscillator Technique, Mater. Sci. Engn. A 442 (2006) 532–537.

38. T.A. Read, The internal friction of single metal crystals. Phys. Rev. 58 (1940) 371-380.

39. S. Hashemizadeh, A. Biancoli, D. Damjanovic, Symmetry breaking in hexagonal and cubic polymorphs of $BaTiO_3$, J. Appl. Phys. 119 (2016) 094105.

40. F. Bai, J.F. Li, D. Viehland, Domain hierarchy in annealed (100)-oriented $Pb(Mg_{1/3}Nb_{2/3})O_3$-x%$PbTiO_3$ single crystals, Appl. Phys. Lett. 85 (2004) 2313-2315.

41. K. Uchino, Chapter 3: Relaxor Ferroelectric-Based Ceramics, In: Advanced Piezoelectric Materials (Second Edition), K. Uchino, Ed., Woodhead Publishing, 2017, 127-153.

42. J.A. Mydosh, Spin glasses: redux: an updated experimental/materials survey, Rep. Prog. Phys. 78 (2015) 052501.

43. G.A. Smolenskii, V.A. Isupov, A.I. Agranovskaya, S.N. Popov, Ferroelectrics with diffuse phase transition, Soviet Physics –Solid State, 2 (1961) 2584-2594.

44. F. Gilletta, M. Chabin, C.-X. An, Thermal properties of lead phosphate, Phys. Stat. Sol. (a) 35 (1976) 545-549.

45. E.K.H. Salje, B. Wruck, Specific-heat measurements and critical exponents of the ferroelastic phase transition in $Pb_3(PO4)_2$ and $Pb_3(P_{1-x}As_xO_4)$, Phys. Rev. B 28 (1983) 6510-6518.

46. N. Novak, R. Pirc, M. Wencka, Z. Kutnjak, High-Resolution Calorimetric Study of $Pb(Mg_{1/3}Nb_{2/3})O_3$ Single Crystal, Phys. Rev. Lett. 109 (2012) 037601.

47. Z. Kutnjak, J. Petzelt, R. Blinc, The giant electromechanical response in ferroelectric relaxors as a critical phenomenon, Nature 448 (2006) 956-959.

48. M.S. Wechsler, D.S. Lieberman, T.A. Read, On the theory of the formation of martensite, Trans. AIME 197 (1953) 1503-1515.

49. D.S. Lieberman, M.S. Wechsler, T.A. Read, Cubic to orthorhombic diffusionless phase change-experimental and theoretical studies of AuCd, J. Appl. Phys. 26 (1955) 473-484.

50. C.C. Chou, C.M. Wayman, Cubic to tetragonal martensitic transformation in lead titanate ($PbTiO_3$) single crystals, Mater. Trans. JIM 33 (1992) 306-317.

51. G. Deng, A. Ding, G. Li, X. Zheng, W. Cheng, P. Qiu, Q. Yin, Martensitelike spontaneous relaxor-normal ferroelectric transformation in $Pb(Zn_{1/3}Nb_{2/3})O_3$-$PbLa(ZrTi)O_3$, J. Appl. Phys. 98 (2005) 094103.

52.P. Wollants, J. R. Roos, and L. Delaey. Thermally- and stress-induced thermoelastic martensitic transformations in the reference frame of equilibrium thermodynamics, Progr. Mater. Sci. 37 (1993) 227–288.

53. C. Seguí, E. Cesari, J. Pons, Phenomenological modelling of the hysteresis loop in the thermoelastic martensitic transformation, Mater. Trans. JIM, 33 (1992) 650-658.

54. A. Amengual, F.C. Lovey, V. Torra, The hysteretic behaviour of a single-interface martensitic transformation in Cu-Zn-Al shape memory alloys, Scripta Met. Mater. 24 (1990) 2241-2246.

55. S.Kustov, J. Rosselló, M.-Ll. Corró, V. Kaminskii, K. Sapozhnikov, A. Saren, A. Sozinov, K. Ullakko, Magnetic domain walls and macroscopic magnetization-related elastic and anelastic effects during premartensitic transition in Ni_2MnGa, Materials, 12 (2019) 376.
56. S. Lee, Z. Liu, M. Kim, C. Randall, Influence of nonstoichiometry on ferroelectric phase transition in BaTiO3, J. Appl. Phys. 101 (2007) 054119.
57. J. Ortín, A. Planes, Overview 68. Thermodynamic analysis of thermal measurements in thermoelastic martensitic transformations, Acta Metal. 36 (1988) 1873-1889.
58. T.B. Massalski, Comments concerning some features of phase diagrams and phase transformations, Mater. Trans. 51 (2010) 583-596.
59. D. E. Laughlin, N. J. Jones, A. J. Schwartz, and T. B. Massalski, Thermally activated martensite: its relationship to non-thermally activated (athermal) martensite, In: G.B. Olson, D.S. Liberman, A. Saxena, Eds., Proceedings ICOMAT-08. Warrendale, (PA), TMS 2009, 141-144.
60. S. Kustov, D. Salas, E. Cesari, R. Santamarta, J. Van Humbeeck, Isothermal and athermal martensitic transformations in Ni-Ti shape memory alloys, Acta mater. 60 (2012) 2578-2592.
61. A.S. Nowick, B.S. Berry, Chapter 14 in: Anelastic relaxation in crystalline solids, Academic Press, NY, 1972.
62. G. Williams, D.C. Watts, Non-symmetrical dielectric relaxation behaviour arising from a simple empirical decay function, Trans. Faraday Soc. 66 (1970) 80–85.